

Dynamic doping and interphase stabilization for cobalt-free and high-voltage Lithium metal batteries

Received: 16 October 2024

Accepted: 12 March 2025

Published online: 21 March 2025



Ziqing Yao ^{1,3}, Tianji Fu^{1,3}, Tao Pan¹, Chongyang Luo¹, Man Pang¹, Shizhao Xiong², Qingpeng Guo¹, Yujie Li , Shuangke Liu , Chunman Zheng  & Weiwei Sun ^{1,3} 

Cobalt-free spinel $\text{LiNi}_{0.5}\text{Mn}_{1.5}\text{O}_4$ (LNMO) positive electrodes, promise high energy density when coupled with lithium negative electrodes, due to the high discharge voltage platform. However, the intrinsic dissolution of Mn in positive electrode, electrolyte decomposition at high voltage, and dendrite growth on lithium severely compromise cycling stability, limiting the practical application. Herein, we propose ferrocene hexafluorophosphate as an electrolyte additive to achieve dynamic doping of Fe^{3+} in positive electrodes during electrochemical cycling. Furthermore, additive molecule preferentially decomposes at both the positive and negative electrode interfaces, forming thin, dense inorganic positive electrode electrolyte interphase and F, P-rich inorganic solid electrolyte interphase respectively, effectively stabilizing electrode interfaces. Consequently, the $\text{Li}|\text{LNMO}$ batteries based on modified electrolytes effectively enhance cycling stability and rate performance at a charge cutoff voltage of 4.9 V and an LNMO pouch cell performs consistently over 160 cycles. Additionally, the efficacy of ferrocene hexafluorophosphate extends beyond LNMO, demonstrating its universal applicability in stabilizing positive electrodes operating at challenging voltages, including $\text{LiNi}_{0.8}\text{Co}_{0.1}\text{Mn}_{0.1}\text{O}_2$, $\text{LiNi}_{0.6}\text{Co}_{0.2}\text{Mn}_{0.2}\text{O}_2$, and LiCoO_2 and a 470 Wh kg^{-1} level Li metal pouch cell was successfully realized.

With the exponential growth in the amount of portable electronic devices, the accelerated pace of electric mobility, and the ambitious objective of global carbon neutrality, there is a pressing need for human civilization to develop large-scale, sustainable, high-energy-density electrochemical energy storage devices^{1–3}. Lithium-ion batteries (LIBs) are currently the most efficient and widely utilized energy storage device⁴. The majority of LIBs currently in use employ transition metal (TM) oxide positive electrodes, including LiCoO_2 (LCO), $\text{LiNi}_x\text{Co}_y\text{Mn}_{1-x-y}\text{O}_2$ (NCM), and LiFePO_4 , etc^{5–8}. However, the pursuit of Co-free and high energy density has led to the emergence of the

disorder $\text{LiNi}_{0.5}\text{Mn}_{1.5}\text{O}_4$ (LNMO) as a prominent contender, attracting the attention of researchers due to its high discharge plateau (4.7 V) and specific energy (650 Wh kg^{-1}) as well as its cost-effective and sustainable attributes^{9,10}. In particular, the outstanding performance of LNMO is even more attractive when coupled with lithium metal negative electrodes to form lithium metal batteries (LMBs), which is regarded as a potential candidate for the forthcoming generation of power cells^{11–13}.

Unfortunately, the route of practical realization of cobalt-free, high-voltage LMBs exemplified by LNMO remains obstructed due to

¹College of Aerospace Science and Engineering, National University of Defense Technology, Changsha, China. ²Department of Materials Science and Engineering, Kunming University of Science and Technology, Kunming, China. ³These authors contributed equally: Ziqing Yao, Tianji Fu, Weiwei Sun.

✉ e-mail: yujieli@nudt.edu.cn; liushuangke@nudt.edu.cn; zhengchunman@nudt.edu.cn; wwsun@nudt.edu.cn

capacity decay during cycling. One mechanism of capacity fade is the dissolution of transition metals from positive electrodes, particularly Mn, which leads to positive electrode degradation and structural collapse at high voltages¹⁴. During the cycling process, Mn³⁺ in the LNMO positive electrode will be disproportionate, generating Mn⁴⁺ and Mn²⁺. Mn²⁺ is easily dissolved in the organic electrolyte, which causes Jahn-Teller effect^{15–18}. Another reason for capacity decay is the occurrence of undesirable and severe side reactions between the electrolyte and the dissolved Mn ions on the positive electrode surface at high voltage, leading to the formation of an unstable positive electrode electrolyte interphase (CEI)^{19–21}. Furthermore, the issue of dendrite growth on lithium-negative electrodes emerges a pivotal challenge, not only compromising the battery performance but also posing a risk of separator puncturing and short circuits within the battery, in extreme cases, safety issues such as thermal runaway^{22–24}.

Previous efforts to improve the cycling stability of Li||LNMO batteries have mainly focused on addressing individual aspects of the above three issues, resulting in varying degrees of success for practical application. For example, Pirmin Stüble et al.²⁵ stabilized the positive electrode lattice structure through Fe and Ti elements co-doping, but the high-temperature annealing consumes a significant amount of energy and results in uneven distribution of the doped elements. Wu et al.²⁶ constructed LiF-rich and LiPO₂F₂-rich anion-derived CEI membranes by a high-concentration electrolyte strategy, which led to a significant enhancement in the cycling stability of LNMO, yet the fluorine-containing solvents are expensive and not environmentally friendly. In addition, Liu et al.²⁷ proposed an ethoxy pentafluoro cyclotriphosphazene additive to synergistically regulate CEI and protect lithium-negative electrodes, but the structural degradation of LNMO remains inevitable. Employing a simple, straightforward, and scalable methodology to comprehensively address all three issues still remains a challenge.

Electrolyte additive engineering provides a simple, effective, and scalable solution to address the stability of the electrode-electrolyte interface, particularly under high-voltage operating conditions^{28,29}. Herein, we introduce a multifunctional electrolyte additive, ferrocene hexafluorophosphate (FHFP), which embodies dual benefits. Initially, FHFP constructs a robust interface enriched with inorganic components at both the positive electrode-electrolyte and lithium negative electrode-electrolyte interphase, bolstering the stability of Bi-electrode interfaces. More crucially, FHFP enables dynamic Fe element doping into the positive electrode lattice during electrochemical cycling, effectively mitigating the dissolution of lattice Mn and consequently reinforcing the structural integrity of the positive electrode lattice.

In this endeavor, we integrate FHFP, a ferrocene salt that contains the same PF₆[−] anion, into the conventional carbonate electrolyte, 1.2 M LiPF₆ in ethylene carbonate/ethyl methyl carbonate (EC/EMC) = 3:7 vol %, tailored for high-voltage LNMO lithium metal batteries. Through theoretical calculations, molecular simulations, a series of electrochemical tests, and various characterization methods, we decipher the intricate mechanisms underpinning the multifaceted effects of FHFP. Firstly, FHFP enables the homogeneous and environmentally benign doping of Fe elements into the positive electrode lattice during cycling, effectively mitigating Mn dissolution and reinforcing positive electrode structural integrity (Fig. 1a). Secondly, it promotes the growth of a thin, uniform, and inorganic-rich CEI, while concurrently refining Li deposition morphology and inhibiting dendrite formation through F, P-rich solid electrolyte interface (SEI) protection (Fig. 1b). Consequently, the FHFP additive not only improves the cycling stability of the LNMO system, but also demonstrates promising universality in enhancing the cycling performance of other high-voltage positive electrode battery systems, encompassing NCM811, NCM622, and LCO chemistries. Moreover, the electrolyte additive enables the 6.51 Ah Li||NCM811 pouch cell to exhibit a specific energy of 470.3 Wh kg^{−1},

delivering a lifespan of 30 cycles under the harsh conditions of a low negative/positive capacity ratio of 1.28 and lean electrolyte of 1.29 g Ah^{−1}.

Results

Structural and physicochemical properties of FHFP additive

FHFP, a sandwich-structured hexafluorophosphate compound (Fig. 2a), encompasses two cyclopentadienyl ligands (Cp, C₅H₅[−]) chelating a Fe³⁺ center (ferrocene ion, Fc⁺) and a PF₆[−] anion. Although the Cp-metal interaction is typically deemed robust, recent research by Münzfeld et al. elucidated its electrostatic nature³⁰, fostering the theoretical feasibility of metal ion detachment under electric fields. As illustrated in Fig. 2b, the electrostatic potential distribution diagrams of FHFP, Fc, and other substances reveal that the positive charge of Fe with respect to Cp in the Fc⁺ structure provides auxiliary evidence of the electrostatic interaction between them. As anticipated, the structural optimization of Fc⁺ at varying electric field strengths demonstrates that the bond length between Fe atom and Cp increases and the bonding strength diminishes as the electric field strength rises. The structure collapses and fails to converge at a higher electric field, indicating that the Fe ions are free under the electric field, which prepares the crystals for doping (Supplementary Fig. 1). Notably, the smaller atomic radius of Fe compared to Ni and Co facilitates lattice doping. In consideration of the preceding pertinent studies on metallocene decomposition, it is feasible to extrapolate the decomposition pathway of Fc⁺ under an electric field, as delineated in Supplementary Fig. 2³¹. Visual inspections of FHFP concentrations in baseline electrolytes reveal full solubility at 0.2 mM (≈0.13% wt), characterized by a distinct blue hue and optimal electrochemical performance (Supplementary Figs. 3, 4). In order to ascertain the effect of the FHFP additive on the thermal performance of the electrolyte, accelerated rate calorimetry (ARC) was employed. The results shown in Supplementary Fig. 5 demonstrated a higher temperature threshold and a slower rate of exotherm generation from the decomposition of the FHFP-modified electrolyte than the baseline electrolyte, which suggests that FHFP has the potential to enhance the thermal stability of the electrolyte. In addition, electrostatic potential (ESP) elucidates the interactions between the solvent and solute anions and cations, thereby predicting the state of the FHFP molecule in the solvent. To unravel the solvent-embedded architecture of FHFP, classical molecular dynamics (CMD) simulations were executed, detailing its solvated conformation and radial distribution of Fc⁺ ions (Fig. 2c and Supplementary Figs. 6, 7). In conjunction with the nuclear magnetic resonance (NMR) analysis, FHFP additives are implicated in mitigating Li⁺ solvation, favorably augmenting electrolyte performance (Supplementary Fig. 8)³². Notably, FHFP improves electrolyte wettability, reducing the separator's contact angle from 19.5° to 15° (Supplementary Fig. 9). The results of the float tests conducted at 5 V high voltage indicate a reduction in leakage current with the FHFP additive (Supplementary Fig. 10). Cyclic voltammetry (CV) test reveals enhanced redox peak areas (Supplementary Fig. 11), while linear scanning voltammetry (LSV) data demonstrate a higher decomposition threshold voltage for FHFP-modified electrolyte versus the baseline electrolyte (Supplementary Fig. 12). Electrochemical impedance spectroscopy (EIS) confirms a marked decrease in battery impedance upon FHFP addition (Supplementary Fig. 13), facilitating Li⁺ transport.

To validate the dynamic doping mechanism of Fe³⁺ in FHFP-modified electrolytes, inductively coupled plasma (ICP) analysis was conducted on the modified electrolyte post-cycling. The ICP results (Fig. 2d and Supplementary Table 1) indicate that the dynamic doping can be roughly divided into three phases. The first phase occurs during the initial 20 to 50 cycles, where Fe substitutes Mn in situ to enter the crystal lattice. Afterward, the contents of Mn and Fe reach equilibrium. When the cycles exceed 150, the Mn content in the electrolyte rises slowly again, during which the FHFP additive sacrifices itself to

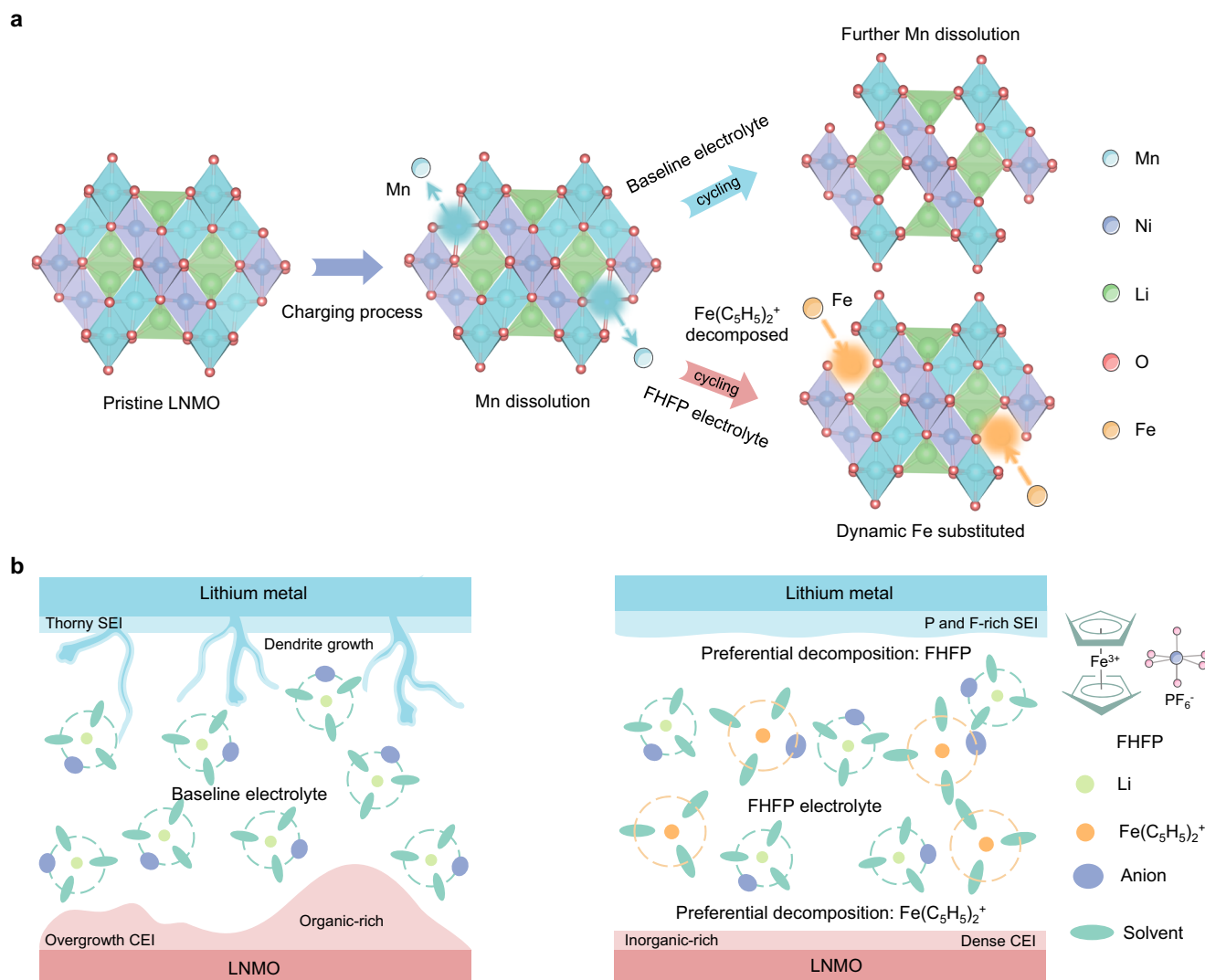


Fig. 1 | Function schematic illustration of FHFP in Li||LNMO cells. a Modification mechanism of FHFP to achieve dynamic doping of Fe at the positive electrode and reduce the structural instability of LNMO caused by Mn dissolution. **b** Mechanism

of CEI and SEI regulation by FHFP. The left is the baseline electrolyte, and the right is the FHFP-modified electrolyte.

compensate for the dissolution of Mn, thereby maintaining structural stability during the cycle. Notably, the reduction in Fe concentration within the electrolyte is more pronounced than the observed increase in Mn. This may be attributed to the involvement of Fe in the formation of solid electrolyte interphase.

In electrolyte evaluations, the highest occupied/lowest unoccupied molecular orbital (HOMO/LUMO) guides decomposition prediction³³. As anticipated, the ferrocene ion is determined to possess the highest HOMO (1.963 eV), indicating its high electron repulsion and preferential oxidation at the positive electrode surface. The FHFP molecule has the lowest LUMO (−3.768 eV), suggesting its high electron affinity and preferential reduction at the lithium negative electrode. Given the face-centered cubic stacking mode of Li metal and the X-ray diffraction pattern of the LNMO positive electrode (Supplementary Fig. 14), Li (110) and LNMO (111) are selected as the optimal adsorption surfaces for the substance. Adsorption energy calculations on Li (110) and LNMO (111) dominated crystal plane highlight the adsorption proficiency of FHFP over other species, with Fc^+ also displaying pronounced adsorption at the positive electrode (Fig. 2f, g and Supplementary Figs. 15, 16). This preferential adsorption enhances FHFP and Fc^+ decomposition, thereby potentiating the effectiveness of the FHFP additive.

Dynamic cation doping and evolution mechanism in LNMO positive electrode

During the electrochemical cycling of LNMO-positive electrodes, a disproportionation reaction of Mn^{3+} occurs, leading to the generation of Mn^{2+} that dissolves into the electrolyte. This dissolution triggers severe Jahn-Teller distortions and structural deterioration. Notably, the incorporation of FHFP as an electrolyte additive facilitates dynamic cation doping, with Fe occupying Mn vacancies (denoted as Fe-LNMO). Double spherical aberration-corrected scanning transmission electron microscopy (STEM) was employed to visualize the atomic occupancies. Comparative analysis between pre-cycling LNMO high angle annular dark field (HAADF) images (Supplementary Fig. 17) and post-cycling LNMO for 50 cycles in baseline electrolyte revealed substantial Mn vacancies (Fig. 3a), whereas samples cycled in FHFP-containing electrolyte exhibited lattice integrity (Fig. 3b). Geometrical phase analysis (GPA) of lattice strain fields subsequent to cycling highlights a pronounced strain accumulation in the baseline electrolyte, absent in FHFP-modified systems, preserving lattice coherence (Supplementary Figs. 18, 19). Owing to the comparable atomic numbers of Fe, Mn, and Ni, the results of the fast Fourier transformation (FFT) are essentially indistinguishable (Supplementary Fig. 20). Further electron energy loss spectra (EELS) analysis revealed an enhancement in Mn-L2,3 edge

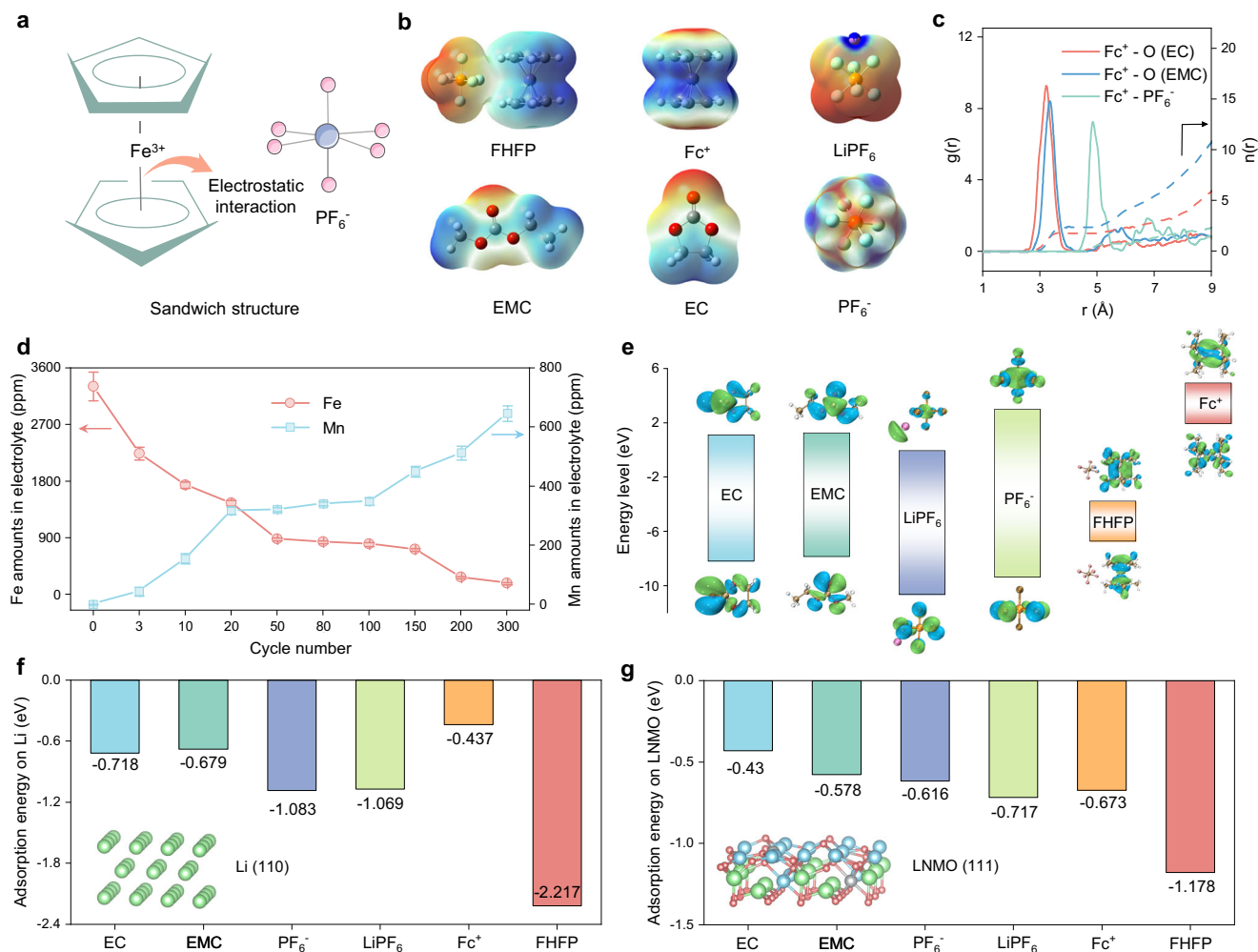


Fig. 2 | Exploration of the effectiveness of FHFP as an electrolyte additive.

a Sandwich structure of FHFP. **b** Electrostatic potential diagrams of the molecules of FHFP, Fc^+ , LiPF_6 , PF_6^- , EMC, EC. Red fields represent negative charge, and blue fields represent positive charge. The gray, red, orange, cyan, green, and blue spheres represent C, O, P, F, H, and Fe atoms, respectively. **c** Radical distribution functions (RDFs, $g(r)$, solid line) and cumulative distribution functions (CDFs, $n(r)$, dashed line) of oxygen and anion around Fc^+ as a function of distance (r) from MD simulations FHFP-modified electrolyte. **d** The amounts of Fe and Mn in the FHFP-

modified electrolyte at different cycles. Electrochemical cycling was performed at a specific current of 73.5 mA g^{-1} . The error bars represent the error obtained from three tests, and the center metric of the error bars is the average of three tests.

e HOMO and LUMO energy levels of EC, EMC, LiPF_6 , PF_6^- , FHFP, Fc^+ . **f**, **g** Adsorption energies of different substances on (f) Li (110) and (g) LNMO (111). The green, red, blue, and gray spheres in the illustration represent Li, O, Mn, and Ni atoms, respectively.

peak intensities with increasing scanning depth from 640 to 642 eV for both pristine and FHFP-cycled LNMO (Fig. 3c, d and Supplementary Fig. 21), indicating a prevalent Mn^{3+} surface layer over a Mn^{4+} bulk phase. Conversely, consistent Mn-L2,3 peak at 642 eV for baseline electrolyte-cycled LNMO underscores detrimental Mn^{3+} dissolution³⁴, emphasizing the role of FHFP in mitigating this issue. Energy dispersive spectrum (EDS) mapping and X-ray photoelectron spectroscopy (XPS) etching spectra of Fe 2p analysis (Fig. 3e, f) confirm a uniform distribution of Fe elements, indicating a homogeneous doping of Fe. Simultaneously, the correlation between Mn and Fe content in the electrolyte versus cycle count (Fig. 2d) underscores the dynamic Fe doping mechanism driven by ferrocene additives during cycling, effectively filling Mn vacancies and hindering further dissolution, thereby enhancing positive electrode stability.

The structural characterization of Fe doping within the material was systematically explored via X-ray absorption fine structure (XAFS) analysis. As illustrated in Fig. 3g, the X-ray absorption near-edge structure (XANES) spectra of Fe K-edge reveals that the valence state of Fe in Fe-doped LNMO closely resembles that of Fe_3O_4 , implying the coexistence of Fe^{2+} and Fe^{3+} species, indicative of partial reduction of

Fe in the FHFP environment. Further examination of the extended X-ray absorption fine structure (EXAFS) spectra analyses clarifies the local coordination environment, with Fe occupying the first shell layer at a Fe-O bond distance of 1.99 \AA , accompanied by a coordination number of 5.4 ± 0.6 , and a second shell layer at 2.94 \AA for Fe-M ($M = \text{Fe}, \text{Mn}, \text{Ni}$) coordination, exhibiting a coordination number of approximately 4.7 ± 1.2 (Fig. 3h, i, Supplementary Figs. 22–24, Table 2, and Note 1). In order to gain further insight into the sites of dynamic doping of Fe, a series of formation energies calculated by DFT was implemented. As illustrated in Supplementary Fig. 25, the formation energies of Fe occupying Mn sites in LNMO and Mn vacancies in LNMO where Mn dissolution occurs are 0.734 eV and -7.664 eV , respectively. These values represent the lowest formation energies across all potential sites, suggesting that there is a heightened likelihood of Fe occupying Mn octahedral sites. Considering the lower formation energy combined with the Fe-O coordination number closer to 6, it is reasonable to assume that as Mn continues to dissolve out of LNMO during electrochemical cycling, Fe dynamically replaces the original Mn octahedral sites, thus mitigating the lattice damage caused by Mn dissolution. Theoretical calculations of the Fe-LNMO system

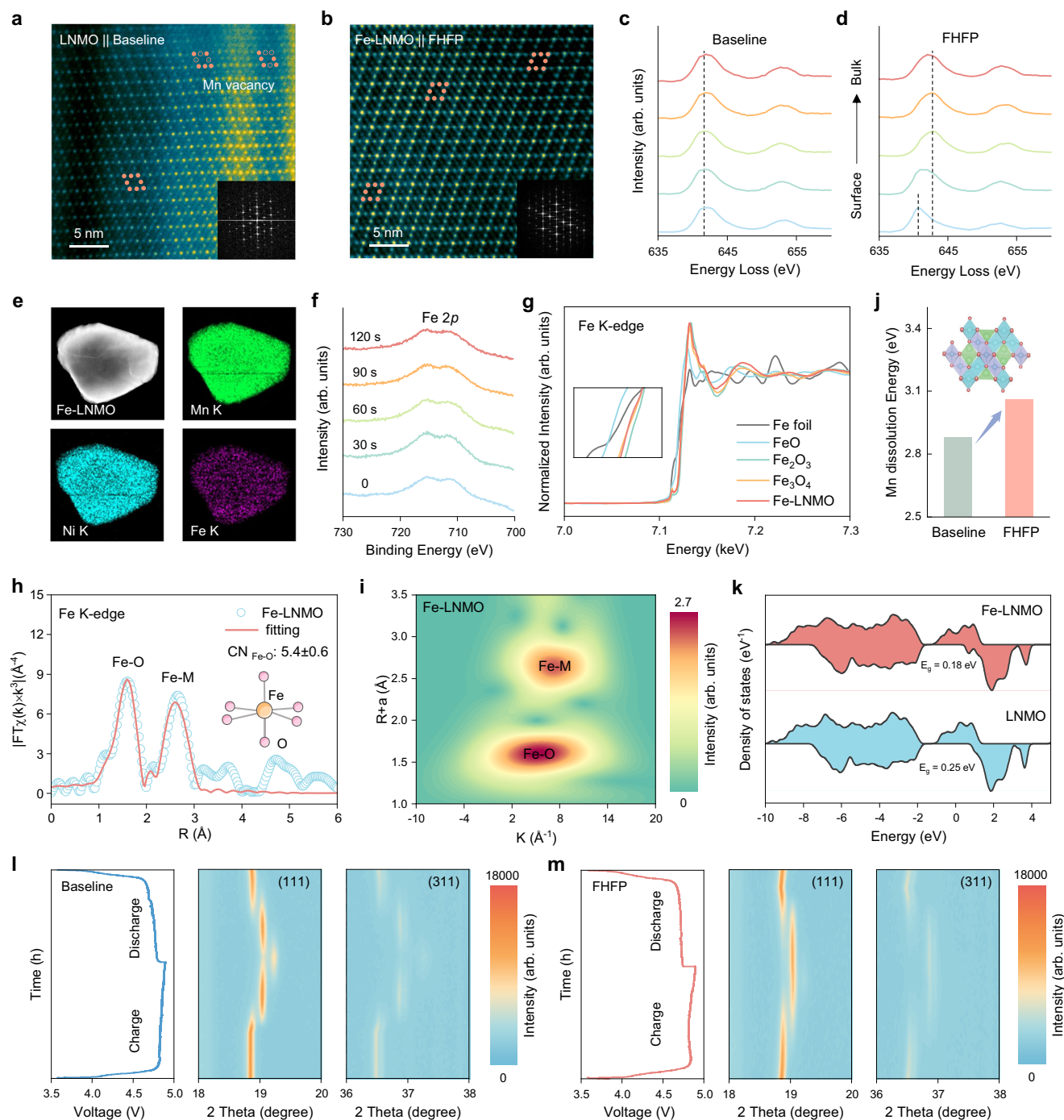


Fig. 3 | Characterizations of Fe-doped enhanced LNMO positive electrodes.

a, b HAADF-STEM of **(a)** LNMO in baseline electrolyte and **(b)** Fe-LNMO in FHFP electrolyte after 50 cycles at 29.4 mA g^{-1} between 3.5–4.9 V (25 °C). The insets are the corresponding FFT patterns. **c, d** EELS Mn L-edge of LNMO in baseline **(c)** and FHFP-modified electrolyte **(d)** after 50 cycles from the surface (0 nm) to the bulk structure (8 nm). **e** The EDS maps of elements in Fe-LNMO. **f** Fe 2p XPS etching spectra of Fe-LNMO in FHFP electrolyte after 50 cycles at 29.4 mA g^{-1} between 3.5–4.9 V (25 °C). **g** Fe K-edge XANES of Fe-LNMO in FHFP electrolyte after 100 cycles at 29.4 mA g^{-1} between 3.5–4.9 V (25 °C). **h** Fourier transform magnitude of Fe K-edge EXAFS spectrum of Fe-LNMO. The inset is a schematic diagram of Fe-O

coordination. **i** Wavelet-transform (WT) image of EXAFS data at Fe K-edge with the optimized Morlet parameter (i.e., $\kappa = 5$, $\sigma = 1$) for Fe-LNMO. **j** Mn dissolution energy of LNMO in the baseline electrolyte and Fe-LNMO in the FHFP-modified electrolytes. The green, red, blue, and purple spheres in the illustration represent Li, O, Mn, and Ni atoms, respectively. **k** Density of states of LNMO before and after Fe doping. **l, m** In situ XRD test contour plots with corresponding charge/discharge curves of LNMO with **(l)** baseline electrolyte and **(m)** FHFP electrolyte after pre-cycling for two cycles at 29.4 mA g^{-1} . In situ XRD tests were operated between 3.5 and 4.9 V at 29.4 mA g^{-1} and 25 °C.

underscore an increase in Mn dissolution energy from 2.88 eV to 3.06 eV upon Fe modification (Fig. 3j), hindering Mn dissolution dynamics. Concurrently, the involvement of Fe d-orbitals in bonding alters the projected density of states (PDOS) in these orbitals, narrowing the band gap from 0.25 eV to 0.18 eV and enhancing intrinsic

conductivity (Fig. 3k and Supplementary Fig. 26). The galvanostatic intermittent titration technique (GITT) analysis presented in Supplementary Fig. 27 demonstrates a substantial enhancement in the Li^+ diffusion coefficient within LNMO positive electrodes, approximately 100-fold higher when cycled in FHFP-modified electrolytes compared

to baseline conditions, which is yet another demonstration that Fe does not occupy the Li site because this situation hinders Li transport. In order to provide direct evidence for the dynamic doping behavior of Fe and its effects, in situ XRD tests were implemented after two cycles of pre-cycling. The results are shown in Fig. 3l–m, where it is evident that attributed to the dissolution of a significant quantity of Mn, the (111) and (311) crystal directions of the LNMO lattice are subject to substantially scarier lattice strains in the baseline electrolyte (Fig. 3l) compared to FHFP-modified electrolyte (Fig. 3m). The FHFP additive facilitates partial doping of Fe elements in the pre-cycling process, and enables dynamic occupation of Mn vacancies by Fe elements in the in situ testing cycle. Consequently, the lattice expansion and contraction is slowed down, and the further dissolution of Mn is inhibited, thereby achieving the effect of lattice stabilization. In combination with the preceding ICP analysis of Fig. 2d, the FHFP additive emerges as an innovative strategy for dynamic, homogeneous Fe doping during electrochemical cycling, reinforcing lattice integrity and stability, while promoting electrical conductivity and Li-ion diffusion in Fe-LNMO positive electrodes. In addition, this approach effectively mitigates Mn leaching, thereby stabilizing battery performance from the positive electrode perspective.

CEI compositions and structural regulation

The time-of-flight secondary ion mass spectrometry (TOF-SIMS) results indicate that the CEI layer in the FHFP-modified electrolyte exhibits markedly reduced TM groups, specifically MnF_2^- and NiF_2^- , in comparison to the baseline electrolyte (Fig. 4a, b), which serve to minimize the occurrence of side reactions between active metal ions and organic solvents. Concurrently, the solvent decomposition product CHO_2^- and anion decomposition product PO_2^- are also observed to be considerably diminished with FHFP (Fig. 4c and Supplementary Fig. 28). To gain further insight into the CEI, XPS etching was performed on the LNMO positive electrode post-cycling in both baseline and FHFP-modified electrolyte. The Fe 2p signal is identified in the CEI of the modified electrolyte (Supplementary Fig. 29). Subsequently, the split-peak fits to F 1s, C 1s, O 1s, and Mn 2p (Fig. 4d, e, Supplementary Fig. 30 and Supplementary Tables 3–5) provide further information of CEI in different electrolyte^{35–37}. The modified electrolyte displays a heightened concentration of LiF at the surface, which typically exhibits chemical and electrochemical inertness during the cycling process, thereby effectively inhibiting further interfacial side reactions. Furthermore, a reduction in the concentration of the PF_6^- decomposition product $\text{Li}_x\text{PF}_{3-x}\text{O}$ and a decrease in the intensity of CO_3^{2-} peaks in the C1s spectrum are also observed under FHFP modification. This suggests that FHFP effectively inhibits electrolyte side reactions. The preferential oxidation of ferrocene ions at the positive electrode is thought to result in the reduction of decomposition of EC and EMC molecules, which in turn leads to a decrease in the organic content of CEI according to the lower ratio of C element in Fig. 4f. Because of fewer organic components and more inorganic components, the FHFP-modified electrolyte has much lower activation energy for the charge transfer process (Supplementary Fig. 31). This is believed to contribute to the favorable electrochemical performance of CEI under the FHFP-modified electrolyte. In parallel, the Mn 2p spectra indicate an increase in Mn^{3+} at the surface of CEI in the modified electrolyte, indicating that the optimized CEI is capable of anchoring Mn^{3+} and preventing its shuttling towards the electrolyte and lithium negative electrode. Nevertheless, the content of Mn at varying depths of the CEI layer in the FHFP-modified electrolyte remains inferior to that of the baseline electrolyte (Supplementary Fig. 32), and this discrepancy may be attributed to the inhibition of Mn dissolution by the additives. Furthermore, in situ EIS was performed at the specific current of 50 mA g^{-1} to characterize the impedance evolution for the interface (Fig. 4g and Supplementary Fig. 33), and the EIS spectra were further analyzed by the distribution of relaxation in time (DRT) tools (Fig. 4h, i

and Supplementary Fig. 34). Distinctly, the in situ EIS spectra in FHFP modified electrolyte are more stable with charging and discharging process due to the durable CEI. According to relaxation time, the total impedance is divided into R_s , R_{CEI} , R_{ct} , and W ^{38,39}. The DRT curves provide a visual representation of the manner in which the four kinds of impedance undergo a confusing change with the charge/discharge process in the baseline electrolyte. In contrast, the presence of FHFP serves to stabilize and reduce the impedance to a much greater extent due to the success of component modulation and optimization in CEI. In addition, the morphology of the LNMO positive electrode under transmission electron microscopy (TEM) after 50 cycles visualizes that the CEI is overgrowth in the baseline electrolyte, whereas it becomes thin and uniform with the FHFP additive (Fig. 4j, k). The rationale behind this phenomenon is that the FHFP additive impedes the dissolution of TM ions and side reactions with electrolytes and further facilitating the formation of an optimal CEI.

Lithium negative electrode interphase and plating/stripping reversibility

The FHFP additive effectively reduces the activation energy for Li^+ transport ($63.53 \text{ kJ mol}^{-1}$) compared to the SEI in the baseline electrolyte ($70.21 \text{ kJ mol}^{-1}$) (Fig. 5a and Supplementary Fig. 35), which will induce a more homogeneous Li deposition morphology. As illustrated in Fig. 5b, c, the EDS spectra of the scanning electron microscope (SEM) of the lithium negative electrode demonstrate that the F and P contents of the SEI formed by the FHFP-modified electrolyte are markedly elevated, suggesting that there is a greater quantity of inorganic material. Furthermore, the surface of the lithium negative electrode in the baseline electrolyte is observed to be fragmented, whereas it is noted to be very flat following modification. A more discernible lithium deposition morphology is shown in Fig. 5d and Supplementary Fig. 36, wherein the lithium deposit morphology transitions from porous dendrites in the baseline electrolyte to dense grains, attributable to the protection of the lithium negative electrode by the FHFP and the lower activation energy for Li^+ diffusion. Typically, a high aspect ratio and specific surface area dendrites result in greater dead Li generation, which in turn leads to diminished coulombic efficiency and battery failure. Importantly, the XPS data demonstrate that the Li negative electrode in the FHFP-modified electrolyte exhibits reduced levels of Mn (Fig. 5e), indicating that the cross-talk effect of TM ions is diminished. Furthermore, the detection of Fe 2p signals and an elevated LiF content in the SEI of the modified electrolyte substantiates the enhanced efficacy of the FHFP additive (Supplementary Figs. 37, 38). It is notable that the peak of Fe 2p is observed at 772 eV, which is markedly different from the peak detected at 715 eV at the LNMO positive electrode. This may be attributed to the preference of FHFP additives to undergo oxidation versus reduction reactions at both the positive electrode and negative electrode. Operando optical microscopy was employed to examine the reversibility of Li plating/stripping (Fig. 5f). It is observed that lithium dendrites emerged on the surface of lithium in the baseline electrolyte at 5 min at a current density of 2 mA cm^{-2} , exhibiting rapid growth and the formation of scary lithium dendrites with a maximum diameter of $430 \mu\text{m}$ by 30 min. In contrast, no dendrites are observed on the surface of Li in the modified electrolyte until 30 min. Meanwhile, it is observed that the blue FHFP exhibits a preferential adhesion to the lithium surface, due to a lower adsorption energy, forming a protective layer. Furthermore, Fig. 5g illustrates the long-term measurements of symmetric Li||Li cells, demonstrating that the battery with the FHFP-modified electrolyte can plate/strip over 640 h at 0.5 mA cm^{-2} and 0.5 mAh cm^{-2} , whereas the battery with the baseline electrolyte fails after only 320 h due to short-circuiting caused by lithium

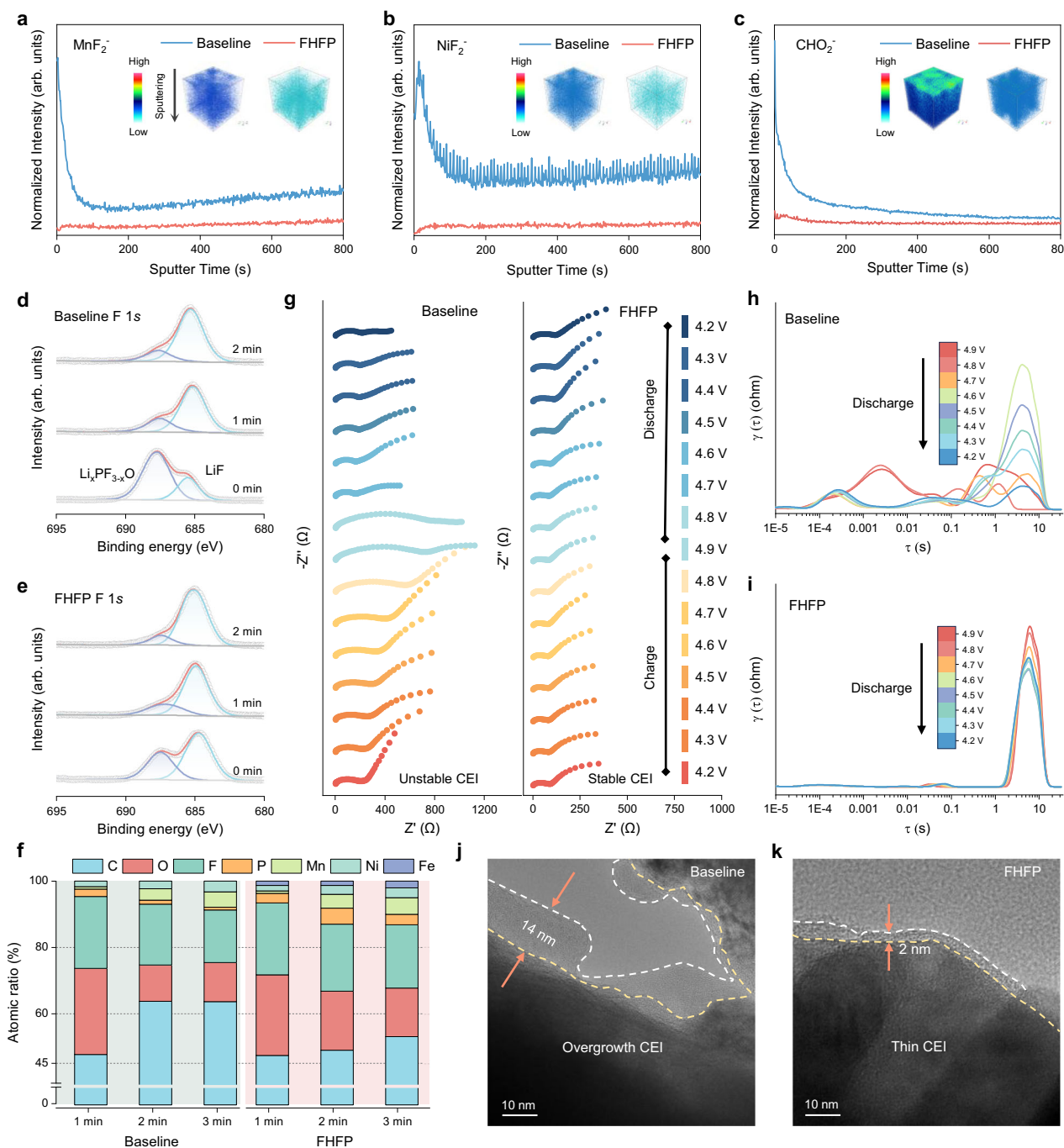


Fig. 4 | Investigation of positive electrode chemistry and CEI stability after 50 cycles in baseline and FHFP-modified electrolytes. **a–c** The intensity depth profiles of TOF-SIMS for (a) MnF_2^- , (b) NiF_2^- , and (c) CHO_2^- fragments on the surface of the LNMO positive electrode after 50 cycles at 29.4 mA g^{-1} between 3.5–4.9 V. The insets are the 3D views of corresponding secondary ions and corresponding scale bars. **d, e** F 1s spectra of the CEI on LNMO after 50 cycles in baseline (d) and FHFP-modified electrolyte (e) at 29.4 mA g^{-1} between 3.5–4.9 V. **f** Atomic contents

derived from the XPS spectra of the CEI on LNMO cycled in different electrolytes. **g** In situ EIS of $\text{Li}||\text{LNMO}$ cells cycled in different electrolytes during charge/discharge at a cutoff voltage of 4.9 V and 29.4 mA g^{-1} (25°C) after 50 cycles at 29.4 mA g^{-1} . **h, i** DRT curves obtained from in situ EIS results during the discharge process in baseline (h) and FHFP-modified electrolyte (i). **j, k** TEM images of LNMO after 50 cycles at 29.4 mA g^{-1} between 3.5–4.9 V in the baseline (j) and FHFP-modified electrolyte (k).

dendrites piercing the separator. These results provide compelling evidence that FHFP additives enhance the reversibility of Li plating/stripping.

Electrochemical performance with different LMBS

The enhancement and universality of FHFP additive for LIBs was evaluated using aggressive positive electrodes, including LNMO (4.9 V), NCM811 (4.7 V), NCM622 (4.5 V) and LiCoO_2 (4.6 V). As

illustrated in Fig. 6a, the capacity retention of the LNMO cell after 400 cycles in the baseline electrolyte is only 32.83%. In contrast, the capacity retention after FHFP modification is enhanced to 87.03%.

In comparison to the baseline electrolyte, the dQ/dV curves (Supplementary Fig. 39) in the FHFP-modified electrolyte exhibit a notable redox peak at approximately 3.95 V, indicative of a reaction involving FHFP. Furthermore, the dQ/dV curves in the modified electrolyte demonstrated a high degree of overlap, a stark contrast to the dispersed

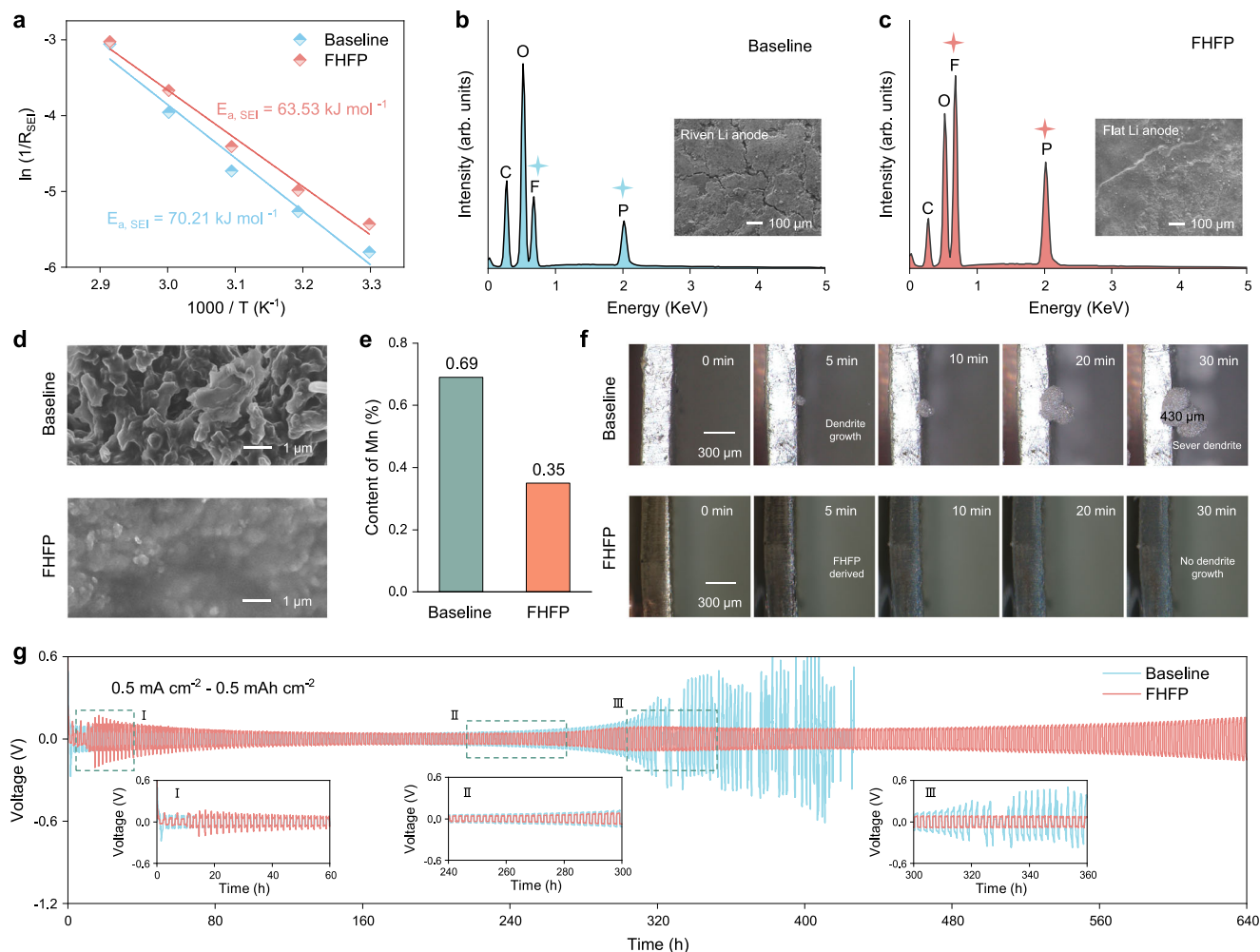


Fig. 5 | Lithium dendrite growth and plating/stripping reversibility in different electrolytes. a Arrhenius plots of the SEI resistance in different electrolytes. **b, c** EDS energy spectra of elements on the surface of Li negative electrode after 50 cycles at 29.4 mA g^{-1} between 3.5–4.9 V in baseline (**b**) and FHFP-modified electrolyte (**c**). The insets show the morphology of the Li-negative electrode after 100 cycles. **d** Morphology of 0.5 mAh cm^{-2} lithium deposit on the Cu current collector in different electrolytes. **e** Mn contents derived from the XPS spectra of the SEI on Li

negative electrode in different electrolytes after 50 cycles at 29.4 mA g^{-1} between 3.5–4.9 V. **f** Operando optical microscopy investigation of the Li plating process on the Li||Li symmetric cells at 2 mA cm^{-2} with different electrolytes. The cutoff capacity is 1 mAh cm^{-2} . **g** Long-term plating/stripping performance of Li||Li symmetric cells at 0.5 mA cm^{-2} and 0.5 mAh cm^{-2} . The illustrations are enlargements of the different stages of the process.

curves observed in the baseline electrolyte. The analysis of the corresponding coulombic efficiency (Supplementary Fig. 40) reveals that the modified electrolyte exhibits lower efficiency at the outset of the cycle (60 cycles), which is attributed to the irreversible redox of FHFP. However, as the cycle progressed, FHFP demonstrates a protective role at both the positive electrode and negative electrode. Subsequently, the coulombic efficiency surpasses that of the baseline electrolyte. Supplementary Fig. 41 illustrates the voltage-capacity curves of the LNMO positive electrode in various electrolytes. It is evident that the charging and discharging curves in the FHFP-modified electrolyte exhibit greater consistency compared to the baseline electrolyte. Additionally, the voltage difference between the charging and discharging platforms is smaller and more stable, suggesting that FHFP is conducive to reducing the polarization voltage of the batteries (Supplementary Fig. 42). Simultaneously, the LNMO coin cell with FHFP additive exhibits a high and stable median voltage of 4.62 V on average for 400 cycles, whereas the average median-voltage in the baseline electrolyte is 4.56 V with a rapid degradation (Supplementary Fig. 43a). Accordingly, FHFP represents a novel approach to enhancing battery energy density. Additionally, the performance investigations at 50°C (Fig. 6b) and 5°C high rate (Supplementary Fig. 44) provide further evidence of the efficacy of the

FHFP additive. It should be noted that the substantially elevated discharge capacity observed in the FHFP-modified electrolyte during the high-temperature test depicted in Fig. 6b is attributed to the dynamic Fe doping facilitated by the FHFP additives, which serves to mitigate the impairment to the crystal lattice caused by Mn dissolution and to ensure the reversible embedding and de-embedding of a considerable number of Li^+ . Moreover, a pouch cell comprising LNMO and $50 \mu\text{m}$ Li foil demonstrates stable cycling for 160 cycles with 96% capacity retention (Fig. 6c), and the structure of Li metal pouch cell is illustrated in Supplementary Fig. 45. Concurrently, the median voltage of the Li||LNMO pouch cell displayed in Supplementary Fig. 43b exhibited stability at 4.7 V over a duration of 160 cycles, exhibiting virtually no degradation. The LNMO positive electrode with FHFP-modified electrolyte also exhibits favorable rate performance (Fig. 6d and Supplementary Fig. 46), particularly 111.1 mAh g^{-1} at 5°C and 82.7 mAh g^{-1} at 10°C , which is far ahead of the baseline electrolyte. It is also noteworthy that this performance is at the forefront of relevant research (Supplementary Fig. 47 and Supplementary Table 6). Furthermore, the stability of the batteries with different electrolytes for long-term storage was assessed by means of isothermal aging experiments at 60°C . As illustrated in Supplementary Fig. 48, the results demonstrate that the initial discharge capacity

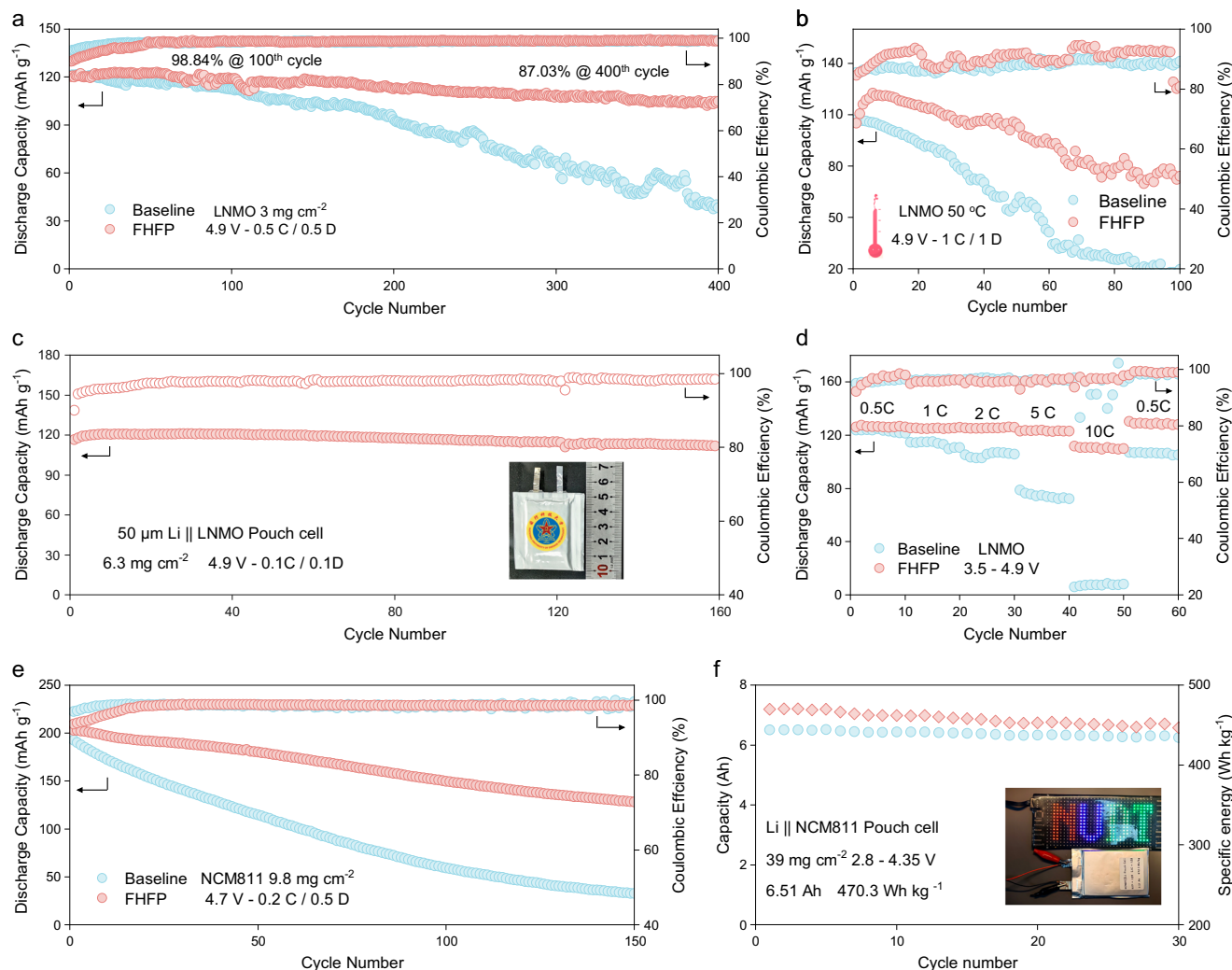


Fig. 6 | Electrochemical performance of different cells with and without FHFP. **a** Cycling performance of Li||LNMO cells at 25 °C between 3.5 and 4.9 V at 0.5 C rate (73.5 mA g⁻¹, 1 C = 147 mA g⁻¹). **b** Cycling performance of Li||LNMO cells at 50 °C and 1 C rate (147 mA g⁻¹). **c** Cycling performance of Li||LNMO pouch cell at 0.1 C rate (14.7 mA g⁻¹) in FHFP-modified electrolyte. The inset is a digital photo of the self-

made pouch cell. **d** Rate performance of Li||LNMO cells. **e** Cycling performance of Li||NCM811 cells between 2.8 and 4.7 V at 0.5 C rate (100 mA g⁻¹, 1 C = 200 mA g⁻¹). **f** Cycling performance of Li||NCM811 pouch cell between 2.8 and 4.35 V at 20 mA g⁻¹.

and cycling performance of the FHFP-modified electrolyte are considerably higher, thereby reflecting the beneficial impact of the FHFP additive strategy on long-term stability. In order to provide further evidence that FHFP contributes to the development of sustainable lithium-ion batteries as an electrolyte additive, it was also employed in NCM811, NCM622, and LCO-positive electrodes and tested at challenging conditions. Figure 6f illustrates the performance of the NCM811 at 4.7 V, which is evident that the capacity decays rapidly due to the inability of the baseline electrolyte to form an effective protection for the positive electrode under an aggressive voltage. In contrast, the cell exhibits 202.8 mA h g⁻¹ specific capacity with FHFP additive, demonstrating enhanced stability. Furthermore, a pouch cell comprising high-loading NCM811 (39 mg cm⁻²) and thin lithium foils (50 μm) was assembled under low negative/positive ratio (N/P = 1.28) and lean FHFP-modified electrolyte (E/C = 1.29) conditions, yielding a capacity of up to 6.51 Ah and high specific energy of 470 Wh kg⁻¹ (Fig. 6g). Besides, the pouch cell was stabilized for over 30 cycles at a specific current of 20 mA g⁻¹ under severe conditions, which is a competitive outcome in the context of existing research on Li metal batteries. The detailed Li||NCM811 pouch cell parameters are presented in Supplementary Fig. 49 and Supplementary Table 7. The techno-economic analysis in Supplementary Fig. 50 demonstrates that the Li||LNMO pouch cell, based on the FHFP-

modified electrolyte, exhibits a substantial cost advantage due to the low cost of LNMO positive electrode and its cycling performance. Moreover, the cost of the Li||NCM811 pouch cell is notably reduced in comparison with previous studies, suggesting that the FHFP additive is a versatile and economical electrolyte modification strategy. In the case of the 4.5 V NCM622 cell, a sharp decline in performance is observed following 40 cycles of stable cycling in the baseline electrolyte, which is indicative of cell failure. Conversely, the cell can undergo 100 stable cycles in the FHFP-modified electrolyte (Supplementary Fig. 51). In addition to Mn-containing transition metal oxide positive electrodes, FHFP has also achieved notable results with LiCoO₂, displaying a cycling capacity over 200 cycles at a high voltage of 4.6 V with 90% capacity retention, as illustrated in Supplementary Fig. 52. Overall, FHFP as an electrolyte additive has been proven to be effective in the case of spinel positive electrode LNMO, as well as in the enhancement of the performance of various other transition metal oxide positive electrodes at high voltages.

Discussion

In this study, we employed the well-known sandwich compound salt ferrocene hexafluorophosphate as an electrolyte additive to lithium-ion batteries with the objective of enhancing the electrochemical performance of various positive electrodes. To this end, we elucidated

the mechanism of action of FHFP using the example of a sustainable Co-free high-voltage positive electrode, LNMO. FHFP is regarded as a universal and efficient electrolyte additive due to its ability to address the prevalent issues of transition metal ions leaching and interface problems associated with transition metal oxide positive electrodes and Li negative electrodes. A series of characterization and theoretical calculations of LNMO cells has revealed that, on the one hand, FHFP will preferentially decompose on both sides due to lower positive electrode/negative electrode adsorption energy and unique HOMO/LUMO, which modulate the interfacial components to form stable inorganic-rich CEI and SEI and inhibit the decomposition of the electrolyte and the dissolution of Mn while cycling. On the other hand, the electrostatic interaction between Fe and the two cyclopentadienyl ligands in FHFP is disrupted at high voltages, which achieves dynamic doping of Fe at different stages of the long cell cycle and compensates for the structural instability brought about by Mn dissolution. The LNMO-assembled coin cell demonstrates 400 stable cycles in the FHFP-modified electrolyte, exhibiting capacity retention of 87%. Furthermore, the pouch cell exhibits high capacity retention of 96% even after 160 cycles. In addition, LNMO exhibits enhanced rate performance in the presence of FHFP, far exceeding the baseline electrolyte. More importantly, for NCM811, NCM622, and LCO positive electrodes at challenging voltages of 4.7 V, 4.5 V, and 4.6 V, respectively, FHFP continues to demonstrate a notable impact, underscoring its versatility as a multifunctional lithium-ion battery electrolyte additive, and contributing to the realization of a lithium-metal pouch cell with a specific energy of 470 Wh kg⁻¹. In conclusion, the combination of dual-interface modulation and positive electrode dynamic doping by FHFP additive has proven successful in addressing the inherent issues of TM oxide positive electrode failure. This strategy has facilitated the practical application of Co-free and high-voltage positive electrodes, such as LNMO, and provided a new electrolyte additive design route for the high energy density and sustainable technology of lithium-ion batteries.

Methods

Electrolytes preparation

The baseline electrolyte was obtained by dissolving 1.2 M LiPF₆ in EC/EMC (3:7 vol%) (DoDoChem), and the FHFP electrolyte was obtained by dissolving a specified quantity of ferrocene hexafluorophosphate additives (0.2 mM, 2 mM, 20 mM) in the baseline electrolyte and stirring for 12 h. The [Fe(C₅H₅)₂]PF₆ was procured from Macklin (Shanghai, China). Reagents were used directly without purification. The preparation of the electrolyte was conducted in an Ar-filled glove box (H₂O < 0.01 ppm, O₂ < 0.01 ppm).

Electrode preparation

LNMO positive electrodes were prepared by mixing the active material, Super P (Canrd Technology Co. Ltd), and binder polyvinylidene fluoride (PVDF, Canrd Technology Co. Ltd) according to 7:2:1 (wt%) and the appropriate amount of N-methyl pyrrolidone (Macklin), ball milled to obtain a slurry, which was coated on aluminum (Al) collector with a 200 μm spatula, and then vacuum-dried in a vacuum oven at 110 °C for 12 h. Then, the as-prepared electrode was cut into a coin shape (12 mm) by hand operated punching tool (WC-HI25, Wellcos Ltd.). The loading mass of the active materials for each LNMO electrode is 1.5–2 mg cm⁻². NCM811, NCM622, and LCO are commercially available electrodes purchased from Canrd Corporation with active substance loadings of 8.66, 20.69, and 10.32 mg cm⁻², respectively. Reagents were used directly without purification.

Batteries assemble

The LNMO, NCM811, NCM622, and LCO electrodes were assembled into a 2032 coin cell (Canrd Technology Co. Ltd). The coin cell was assembled by stacking a 300 μm lithium negative electrode (Canrd

Technology Co. Ltd, >99.9%), separator (Celgard Co.), and electrode by adding 80 μl electrolyte in an Ar-filled glove box (H₂O < 0.01 ppm, O₂ < 0.01 ppm). The separator has a thickness of 25 microns, a diameter of 19 mm, and a porosity and average pore size of 55% and 64 nm, respectively. Li symmetric cells were assembled in the same way as full cells, except that the electrodes were replaced by lithium wafers with a diameter of 15 mm. The Li||LNMO pouch cell was made from 16 cm × 3 cm double-sided coated LNMO electrodes, separator, 0.36 g FHFP-modified electrolyte, and 18 cm × 3 cm × 50 μm lithium tape coil. Al lugs were pressure-welded to the LNMO pole pieces, and Ni lugs were clamped to the lithium tape coil. The prepared cells were encapsulated using an Al-plastic film. The NCM811 pouch cell is assembled using the same method, and the relevant material parameters are provided in Supplementary Table 7. Pouch cells are evacuated and sealed prior to liquid injection, then electrolyte is injected through a syringe in a glove box and sealed a second time.

Electrochemical measurements

The charge/discharge test was conducted on a Neware battery testing system (CT-4008) in a specific potential range for different batteries. Approximately 0.1 MPa of pressure is applied using fixtures throughout the pouch cell testing process. Ex situ/in situ EIS were collected with a perturbation of 10 mV in the frequency range from 0.1 Hz to 1 MHz on an electrochemical workstation (Zennium XC, Zahner). All EIS tests were performed in potentiostatic mode and were held at open circuit voltage for 10 h prior to measurement, generating approximately 60 data points per measurement. The relaxation times in EIS spectra were fitted by the DRT tool developed by Wan et al.⁴⁰. CV tests at different sweep rates were performed on an electrochemical workstation (Autolab PGSTAT-302N, Metrohm). The floating test (chronoamperometry) was evaluated by holding the LNMO electrodes at a constant charge voltage of 5 V for 2 h. GITT curves were tested with constant current (29.4 mA g⁻¹) for 15 min followed by 60 min of relaxation in the voltage range of 3.5–4.9 V on a Land electrochemical testing system. The isothermal aging test involves the accelerated aging of the battery at a temperature of 60 °C for a period of 10 days prior to the commencement of the test procedure. All electrochemical tests were carried out in an air-conditioned room with a temperature value of 25 ± 3 °C.

Materials characterization

The morphology of materials was observed by scanning electron microscope (SEM) with a JEOL JSM 7500 instrument and aberration-corrected scanning transmission electron microscopy (STEM) with a JEOL ARM-200F instrument, where the energy dispersive spectroscopy (EDS) was acquired to determine the element distribution. Aberration-corrected STEM was carried out in HAADF mode on the JEOL ARM-200F instrument. STEM-EELS data was collected in dual-EELS mode to obtain both zero-loss spectra and core-loss spectra, which were calibrated by corresponding zero-loss EELS spectra before analysis. All EELS spectra were processed after subtracting background by the Digital Micrograph (DM) software. The geometric phase analysis (GPA) was conducted by the Strain++ open-source software package developed by J.J.P. Peters⁴¹. The accelerated rate calorimetry (ARC) test was carried out in the heat-wait-search mode with the ARCSYS-777 instrument. An inductively coupled plasma optical emission spectrometer (ICP-OES) (IRIS Intrepid II XSP, Thermo Fisher, USA) was utilized to evaluate the element contents. The surface chemistries of electrodes after cycling were detected by X-ray photoelectron spectroscopy (XPS, Thermo ESCALAB 250Xi) and time of flight secondary ion mass spectrometry (TOF-SIMS, TOF.SIMS 5-100). Signal intensities of all species in TOF-SIMS have been normalized. ¹H, ⁷Li, and ¹⁹F NMR were performed on a Bruker Avance III HD600 MHz at room temperature using CDCl₃ as a solvent. In situ, XRD measurement on LNMO cells with baseline electrolyte and FHFP-modified electrolyte was performed on

a Bruker X-ray diffractometer, and the cells were operated between 3.5 and 4.9 V at a rate of 0.2 C after two pre-cycles. All tests were conducted at $25 \pm 3^\circ\text{C}$ if not otherwise specified.

XAFS

X-ray absorption fine structures (XAFS) of the Fe K-edge were detected at the beamline BL14W1 in Shanghai Synchrotron Radiation Facility (SSRF) in the transmission mode. The LNMO electrodes used in the experiments were first extracted from coin cells (after 100 cycles at 29.4 mA g^{-1}) and cleaned with EMC solution before use. The electrodes were prepared in a glove box and transferred under a vacuum. All operations were performed at $25 \pm 3^\circ\text{C}$. Energy calibration was performed by simultaneously measuring the spectra of a reference metal foil. The raw data were processed and analyzed using the Athena software package. Data process and analysis were carried out using the Demeter program pack with Athena.

Computational details

The density of state, adsorption energy, and dissolution energy of Mn are performed in the framework of the density functional theory with the projector augmented plane-wave method, as implemented in the Vienna ab initio simulation package^{42,43}. The generalized gradient approximation proposed by Perdew-Burke-Ernzerhof (PBE) is selected for the exchange-correlation potential^{44,45}. The cut-off energy for the plane wave is set to 480 eV. The energy criterion is set to 10^{-4} eV in the iterative solution of the Kohn-Sham equation. To avoid interlaminar interactions, a vacuum spacing of 20 Å is applied perpendicular to the slab. The Brillouin zone integration is performed using a $2 \times 2 \times 1$ k-mesh. All the structures are relaxed until the residual forces on the atoms have declined to less than 0.05 eV Å^{-1} . Data analysis and visualization are carried out with the help of VASPKIT⁴⁶ code and VESTA⁴⁷. To make an accurate description of the electronic density of state (DOS), a DFT + U approximation and set U_{eff} to $U(\text{Mn}) = 3.9\text{ eV}$ and $U(\text{Ni}) = 6.2\text{ eV}$ were used. Structure files related to DOS calculations are provided in Supplementary Data 1. The absorption energy (E_{ad}) of different substances on LNMO (111) and Li (110) crystal surfaces were calculated by the following equation:

$$E_{\text{ad}} = E_{\text{base+sub}} - E_{\text{sub}} - E_{\text{base}} \quad (1)$$

Where $E_{\text{base+sub}}$ is the total energy of the adsorbed substrate with adsorbed substance, E_{sub} is the total energy of the adsorbed substance, and E_{base} is the total energy of the adsorbed substrate. The structures of Li negative electrode and LNMO positive electrode adsorbing different molecules are provided in Supplementary Data 2, 3, respectively. The dissolution energy of Mn was calculated by the following equation:

$$E_{\text{d}} = E_{\text{bulk}} - E_{\text{product}} - \mu_{\text{Mn}} \quad (2)$$

where E_{d} is the dissolution energy of Mn, E_{bulk} is the total energy of a fully relaxed bulk structure, E_{product} is the total energy of a fully relaxed product with one Mn atom dissociated, and μ_{Mn} is the chemical potential of the Mn atom. The formation energy structure of Mn vacancies before and after Fe doping is provided in Supplementary Data 4. The formation energies (ΔE_{f}) of the various sites of Fe substitution were calculated using the following equation:

$$\Delta E_{\text{f}(\text{substrate}-\text{Fe})} = E_{(\text{substrate}-\text{Fe})} - E_{\text{f}(\text{substrate})} - \mu_{\text{Fe}} + \mu_{(\text{substituted atom})} \quad (3)$$

where the substrate is LNMO or LNMO containing Mn vacancies, and the substituted atoms are Li, Ni, and Mn. The calculation of the formation energy of Fe occupying Mn vacancies does not include the final term.

The HOMO/LUMO was calculated in the Gaussian 16 program with Becke's three-parameter hybrid method using the Lee-Yang-Parr correlation functional (B3LYP), and 6-311 G (d, p) was chosen as the series basis. Data analysis and visualization are carried out with the help of VMD⁴⁸ and Multiwfn⁴⁹. The electrostatic potential calculations were also conducted with Gaussian 16. All optimizations and frequencies were calculated at the level of TPSSh/Ma-TZVP. Frequency analysis was performed to ensure the ground state of molecular structures. A dispersion correction was also considered using the Becke-Johnson damping function. The solvent-solute interaction was considered with the universal solvation model of SMD⁵⁰. The structures of the different molecules calculated for HOMO-LUMO are provided in Supplementary Data 5.

The solvation structure of the FHFP-modified electrolyte was simulated using the classical molecular dynamics (CMD) method, implemented in the GROMACS 2018.3^{51,52} software package with the OPLS-AA force field⁵³. The Verlet algorithm was employed to solve the Newton equation of motion for the system. The simulation time step was set at 2 fs, and the truncation radius for both electrostatic and van der Waals interactions was set at 1.0 nm. The long-range electrostatic interactions were calculated using the particle mesh Ewald (PME) method. The temperature of the velocity-rescale hot bath control system is 298.15 K, and the pressure of the Parrinello-Rahman pressure bath control system is 1 atm, thus ensuring the system's full stability. In the equilibrium phase of the simulation, the energy of the system was minimized using the conjugate gradient method. This was followed by an equilibrium simulation under the NPT ensemble for 5 ns, and then under the NVT ensemble for a further 5 ns. Finally, the simulation was continued for 20 ns under the NVT ensemble, with data collected throughout. Data analysis and visualization were carried out using VMD⁵⁵. Models for solvated structure calculations are provided in Supplementary Data 6.

Data availability

All the relevant data are included in this article and the Supplementary Information. All other relevant data supporting findings are available from the corresponding author on request. Source data are provided in this paper.

References

- Castelvecchi, D. & Stoye, E. World-changing batteries win Nobel. *Nature* **574**, 308 (2019).
- Zhou, G., Chen, H. & Cui, Y. Formulating energy density for designing practical lithium-sulfur batteries. *Nat. Energy* **7**, 312–319 (2022).
- Xia, Y. et al. Designing an asymmetric ether-like lithium salt to enable fast-cycling high-energy lithium metal batteries. *Nat. Energy* **8**, 934–945 (2023).
- Choi, J. W. & Aurbach, D. Promise and reality of post-lithium-ion batteries with high energy densities. *Nat. Rev. Mater.* **1**, 16013 (2016).
- Dong, Y. & Li, J. Oxide positive electrodes: Functions, instabilities, self healing, and degradation mitigations. *Chem. Rev.* **123**, 811–833 (2023).
- Lee, S., Su, L., Mesnier, A., Cui, Z. & Manthiram, A. Cracking vs. surface reactivity in high-nickel positive electrodes for lithium-ion batteries. *Joule* **7**, 2430–2444 (2023).
- Jia, K. et al. Long-life regenerated LiFePO_4 from spent positive electrode by elevating the d-band center of Fe. *Adv. Mater.* **35**, 2208034 (2023).
- Yao, Z. et al. Modulating the spin state to stabilize the surface and bulk structure for durable 4.6 V LiCoO_2 positive electrodes. *Adv. Funct. Mater.* **34**, 2408152 (2024).
- Zhang, R. Compositionally complex doping for zero-strain zero-cobalt layered positive electrodes. *Nature* **610**, 67–73 (2022).

10. Mao, J. et al. Insights into Lithium inventory quantification of $\text{LiNi}_{0.5}\text{Mn}_{1.5}\text{O}_4$ -graphite full cells. *Energy Environ. Sci.* **11**, 772–799 (2024).
11. Lin, D. Reviving the lithium metal negative electrode for high-energy batteries. *Nat. Nanotechnol.* **12**, (2017).
12. Piao, J.-Y. et al. Phase control on surface for the stabilization of high energy positive electrode materials of lithium ion batteries. *J. Am. Chem. Soc.* **141**, 4900–4907 (2019).
13. Zhang, W. et al. Engineering a passivating electric double layer for high performance lithium metal batteries. *Nat. Commun.* **13**, 2029 (2022).
14. Fu, T. et al. Advances in modification methods and the future prospects of high-voltage spinel $\text{LiNi}_{0.5}\text{Mn}_{1.5}\text{O}_4$ - a review. *J. Mater. Chem. A* **11**, 13889–13915 (2023).
15. Eum, D. et al. Electrochemomechanical failure in layered oxide positive electrodes caused by rotational stacking faults. *Nat. Mater.* **23**, 1093–1099 (2024).
16. Asl, H. Y. & Manthiram, A. Reining in dissolved transition-metal ions. *Science* **369**, 140–141 (2020).
17. Xiao, B. et al. Nanoscale manipulation of spinel Lithium nickel manganese oxide surface by multisite Ti occupation as high-performance positive electrode. *Adv. Mater.* **29**, 1703764 (2017).
18. Kim, J.-H., Yoon, C. S., Myung, S.-T., Prakash, J. & Sun, Y.-K. Phase transitions in $\text{Li}_{1-x}\text{Ni}_{0.5}\text{Mn}_{1.5}\text{O}_4$ during cycling at 5 V. *Electrochem. Solid State Lett.* **7**, A216 (2004).
19. Fan, X. & Wang, C. High-voltage liquid electrolytes for Li batteries: progress and perspectives. *Chem. Soc. Rev.* **50**, 10486–10566 (2021).
20. Jiao, X., Rao, L., Yap, J., Yu, C.-Y. & Kim, J.-H. Stabilizing positive electrode-electrolyte interphase of $\text{LiNi}_{0.5}\text{Mn}_{1.5}\text{O}_4$ high-voltage spinel by blending garnet solid electrolyte in lithium-ion batteries. *J. Power Sources* **561**, 232748 (2023).
21. Hou, W. et al. Rational molecular design of electrolyte additive endows stable cycling performance of cobalt-free 5 V-class lithium metal batteries. *Energy Environ. Sci.* **17**, 8325–8336 (2024).
22. Jagger, B. & Pasta, M. Solid electrolyte interphases in lithium metal batteries. *Joule* **7**, 2228–2244 (2023).
23. Liu, Y. et al. Self-assembled monolayers direct a LiF-rich interphase toward long-life lithium metal batteries. *Science* **375**, 739–745 (2022).
24. Zhang, H., Wang, L. & He, X. Trends in a study on thermal runaway mechanism of lithium-ion battery with $\text{LiNi}_x\text{Mn}_y\text{Co}_{1-x-y}\text{O}_2$ positive electrode materials. *Battery Energy* **1**, 20210011 (2022).
25. Stüble, P., Geßwein, H., Indris, S., Müller, M. & Binder, J. R. On the electrochemical properties of the Fe-Ti doped LNMO material $\text{LiNi}_{0.5}\text{Mn}_{1.37}\text{Fe}_{0.1}\text{Ti}_{0.03}\text{O}_{3.95}$. *J. Mater. Chem. A* **10**, 9010–9024 (2022).
26. Wu, S. et al. Inhibition of transition-metal dissolution with an inert soluble product interface constructed by high-concentration electrolyte. *iScience* **26**, 107052 (2023).
27. Liu, Q. Cooperative stabilization of bi-electrodes with robust interphases for high-voltage lithium-metal batteries. *Energy Storage Mater.* **37**, 521–529 (2021).
28. Zhou, P. et al. Rational Lithium salt molecule tuning for fast charging/discharging Lithium metal battery. *Angew. Chem. Int. Ed.* **63**, e202316717 (2024).
29. Lu, Y. et al. Breaking the molecular symmetry of sulfonimide anions for high-performance lithium metal batteries under extreme cycling conditions. *Nat. Energy* **10**, 191–204 (2025).
30. Münzfeld, L. et al. Synthesis and properties of cyclic sandwich compounds. *Nature* **620**, 92–96 (2023).
31. Cha, Y. et al. Mechanochemistry of cationic cobaltocenium mechanophore. *J. Am. Chem. Soc.* **143**, 11871–11878 (2021).
32. Lu, D. et al. Ligand-channel-enabled ultrafast Li-ion conduction. *Nature* **627**, 101–107 (2024).
33. Peljo, P. & Girault, H. H. Electrochemical potential window of battery electrolytes: the HOMO-LUMO misconception. *Energy Environ. Sci.* **11**, 2306–2309 (2018).
34. Fu, T. et al. Enhancing orbital interaction in spinel $\text{LiNi}_{0.5}\text{Mn}_{1.5}\text{O}_4$ positive electrode for high-voltage and high-rate Li-ion batteries. *Small* **20**, 2402339 (2024).
35. Zhu, X. et al. Epitaxial growth of an atom-thin layer on a $\text{LiNi}_{0.5}\text{Mn}_{1.5}\text{O}_4$ positive electrode for stable Li-ion battery cycling. *Nat. Commun.* **13**, 1565 (2022).
36. Zhang, J.-N. et al. Dynamic evolution of positive electrode electrolyte interphase (CEI) on high voltage LiCoO_2 positive electrode and its interaction with Li negative electrode. *Energy Storage Mater.* **14**, 1–7 (2018).
37. Yabuuchi, N., Yoshii, K., Myung, S.-T., Nakai, I. & Komaba, S. Detailed studies of a high-capacity electrode material for rechargeable batteries, Li_2MnO_3 - $\text{LiCo}_{1/3}\text{Ni}_{1/3}\text{Mn}_{1/3}\text{O}_2$. *J. Am. Chem. Soc.* **133**, 4404–4419 (2011).
38. Lu, Y., Zhao, C.-Z., Huang, J.-Q. & Zhang, Q. The timescale identification decoupling complicated kinetic processes in lithium batteries. *Joule* **6**, 1172–1198 (2022).
39. Li, Z. et al. Electrolyte design enables rechargeable LiFePO_4 /graphite batteries from -80°C to 80°C . *Angew. Chem. Int. Ed.* **64**, e202409409 (2024).
40. Wan, T. H., Saccoccio, M., Chen, C. & Ciucci, F. Influence of the discretization methods on the distribution of relaxation times deconvolution: Implementing radial basis functions with DRTtools. *Electrochim. Acta* **184**, 483–499 (2015).
41. Hÿtch, M. J., Snoeck, E. & Kilaas, R. Quantitative measurement of displacement and strain fields from HREM micrographs. *Ultra-microscopy* **74**, 131–146 (1998).
42. Kresse, G. & Hafner, J. Ab initio molecular dynamics for open-shell transition metals. *Phys. Rev. B* **48**, 13115–13118 (1993).
43. Kresse, G. & Furthmüller, J. Efficient iterative schemes for ab initio total-energy calculations using a plane-wave basis set. *Phys. Rev. B* **54**, 11169–11186 (1996).
44. Perdew, J. P., Burke, K. & Ernzerhof, M. Generalized gradient approximation made simple. *Phys. Rev. Lett.* **77**, 3865–3868 (1996).
45. Kohn, W. & Sham, L. J. Self-consistent equations including exchange and correlation effects. *Phys. Rev.* **140**, A1133–A1138 (1965).
46. Wang, V., Xu, N., Liu, J.-C., Tang, G. & Geng, W.-T. VASPKit: A user-friendly interface facilitating high-throughput computing and analysis using VASP code. *Comput. Phys. Commun.* **267**, 108033 (2021).
47. Momma, K. & Izumi, F. VESTA: a three-dimensional visualization system for electronic and structural analysis. *J. Appl. Crystallogr.* **41**, 653–658 (2008).
48. Humphrey, W., Dalke, A. & Schulten, K. VMD: Visual molecular dynamics. *J. Mol. Graph.* **14**, 33–38 (1996).
49. Lu, T. & Chen, F. Multiwfn: A multifunctional wavefunction analyzer. *J. Comput. Chem.* **33**, 580–592 (2012).
50. Marenich, A. V., Cramer, C. J. & Truhlar, D. G. Universal solvation model based on solute electron density and on a continuum model of the solvent defined by the bulk dielectric constant and atomic surface tensions. *J. Phys. Chem. B* **113**, 6378–6396 (2009).
51. Pronk, S. et al. GROMACS 4.5: a high-throughput and highly parallel open source molecular simulation toolkit. *Bioinformatics* **29**, 845–854 (2013).
52. *Solving Software Challenges for Exascale: International Conference on Exascale Applications and Software, EASC 2014, Stockholm, Sweden, April 2-3, 2014, Revised Selected Papers.* vol. 8759 (Springer International Publishing, Cham, 2015).
53. Jorgensen, W. L. & Tirado-Rives, J. Potential energy functions for atomic-level simulations of water and organic and biomolecular systems. *Proc. Natl. Acad. Sci. USA* **102**, 6665–6670 (2005).

Acknowledgements

The authors acknowledge the financial support from the high-level innovation talent training plan of the National University of Defense Technology (W.S.) and the partial financial support from the National Natural Science Foundation of China (22479067, S.X.).

Author contributions

W.S., S.L., Y.L., and C.Z. conceived and designed the project. Z.Y. performed most experiments and interpreted the data. T.F. performed material characterization tests and made important contributions to DFT calculations. T.P. and C.L. contributed to electrochemical measurements and analyzed the data. M.P. helped with the electrochemical data analysis. S.X. and Q.G. contributed to helpful discussions. W.S. and C.Z. supervised the project implementation. S.L. and Y.L. contributed to polish the article. Z.Y. and W.S. co-wrote the manuscript with contributions from all co-authors. Z.Y., T.F., and W.S. contributed equally. All authors have given approval to the final version of the manuscript.

Competing interests

The authors declare no competing interests.

Additional information

Supplementary information The online version contains supplementary material available at <https://doi.org/10.1038/s41467-025-58110-z>.

Correspondence and requests for materials should be addressed to Yujie Li, Shuangke Liu, Chunman Zheng or Weiwei Sun.

Peer review information *Nature Communications* thanks Kai Liu, and the other anonymous reviewer(s) for their contribution to the peer review of this work. A peer review file is available.

Reprints and permissions information is available at <http://www.nature.com/reprints>

Publisher's note Springer Nature remains neutral with regard to jurisdictional claims in published maps and institutional affiliations.

Open Access This article is licensed under a Creative Commons Attribution-NonCommercial-NoDerivatives 4.0 International License, which permits any non-commercial use, sharing, distribution and reproduction in any medium or format, as long as you give appropriate credit to the original author(s) and the source, provide a link to the Creative Commons licence, and indicate if you modified the licensed material. You do not have permission under this licence to share adapted material derived from this article or parts of it. The images or other third party material in this article are included in the article's Creative Commons licence, unless indicated otherwise in a credit line to the material. If material is not included in the article's Creative Commons licence and your intended use is not permitted by statutory regulation or exceeds the permitted use, you will need to obtain permission directly from the copyright holder. To view a copy of this licence, visit <http://creativecommons.org/licenses/by-nc-nd/4.0/>.

© The Author(s) 2025